Encoding information onto the charge and spin state of a paramagnetic atom using MgO tunneling spintronics

Mathieu Lamblin, ^{1, a)} Victor Da Costa, ¹ Loic Joly, ¹ Bhavishya Chowrira, ¹ Léo Petitdemange, ² Bertrand Vileno, ³ Romain Bernard, ¹ Benoit Gobaut, ¹ Samy Boukari, ¹ Wolfgang Weber, ¹ Michel Hehn, ² Daniel Lacour, ² and Martin Bowen ¹

1) Institut de Physique et Chimie des Matériaux de Strasbourg, UMR 7504 CNRS, Université de Strasbourg, 23 Rue du Læss, BP 43, 67034 Strasbourg, France

2) Institut Jean Lamour UMR 7198 CNRS Université de Lorraine BP 70239, Vandoeuvre les Nancy 54506, France

3) Institut de Chimie UMR 7177 CNRS Université de Strasbourg 4 Rue Blaise Pascal, CS 90032, Strasbourg 67081, France

(Dated: March 17, 2025)

An electrical current that flows across individual atoms can generate exotic quantum transport signatures in model junctions built using atomic tip or lateral techniques. So far, however, a viable industrial pathway for atom-driven devices has been lacking. Here, we demonstrate that a commercialized device platform can fill this nanotechnological gap. According to conducting tip atomic force microscopy, inserting C atoms into the MgO barrier of a magnetic tunnel junction generates nanotransport paths. Within magnetotransport experiments, this results in quantum interferences, and in Pauli spin blockade effects linked to tunneling magnetoresistance peaks that can be electrically controlled. We report an additional persistent memory effect that we attribute to the charging of a single "gating" C atom that is adjacent to a single C atom forming the microscale junction's effective nanotranport path. Local magnetometry experiments confirm the secondary role of magnetic stray fields on the C atoms. Our results show that, to exhibit atom-level properties, a device need not be nanoscaled, and position MgO tunneling spintronics as a promising platform to industrially implement quantum technologies.

Fundamental research on model atomic and molecular junctions has strongly progressed in the last two decades thanks to atomic tip and lateral junction building techniques¹⁻³. Although these technical approaches do not promote industrial nanotechnologies, they have helped reveal intriguing electronic transport mechanisms. Among them are Coulomb blockade inside single-atom transistors⁴, Coulomb drag and co-tunneling effects in capacitively coupled quantum dots⁵, Franck-Condon blockade within carbon nanotubes⁶, spin-phonon coupling in single-molecule magnets⁷, Kondo effect with spinoriented molecules⁸, memristance and hysteresis linked to resistive switching^{9,10} and strong current fluctuations caused by vibrational coupling and structural changes¹¹. More recently, quantum phenomena involving internal coherence and superposition have been reported, such as phonon interference¹², quantum interference and $decoherence^{13}$.

If 3d metal or 2D van der Waals ferromagnetic electrodes are used to establish a fixed spin referential, then the resulting vertical or lateral spintronic device can better exploit the electron spin to examine Coulomb blockade $^{14-16}$, encode quantum information 17 or harvest thermal energy using discrete spin states 18,19 . While molecules offer elegant means of inserting atom-level electronic states within a device, molecular spintronic technologies are still rather rudimentary and thus very far from industrial deployment 17,20 . Finally, much research

has focused on transposing robust state changes to a junction's spintronic response from more exotic barriers such as ${\rm SrTiO_3}^{21}$ to the most widely developed industrial spintronic platform: the FeCoB/MgO/FeCoB magnetic tunnel junction (MTJ), with applications ranging from next-generation memories²² and neuromorphic computing²³ to agile microwave emitters and artificial energy harvesting²⁴.

In this paper, we demonstrate several of the aforementioned atomic transport effects using the industrialization vector that is MgO tunneling spintronics²². Prior literature on MgO tunneling indicates that structural defects can generate localized states within the tunnel barrier^{25–30}. The oxygen vacancies within the tunnel barrier generate discrete electronic states that play a role in spin transfer torque³⁰, and which we have identified²⁹ and controlled^{31–33} in our MgO junctions. These oxygen vacancies are diamagnetic. To achieve discrete, unpaired electron spin states, we introduce carbon atoms onto these oxygen vacancies¹⁸ (see Methods). These states, and the nanotransport paths they promote across the MgO MTJ, are schematized in Fig. 1(a).

I. C-BORNE NANOTRANSPORT PATHS ACROSS A MGO TUNNEL BARRIER

We first use conducting Atomic Force Microscopy (AFM) to examine how inserting C alters the nanoscale conductivity across the MgO barrier (see Methods). When C is absent (Fig. 1(b)), no measurable current is

a) Electronic mail: mathieu.lamblin@lpmmc.cnrs.fr

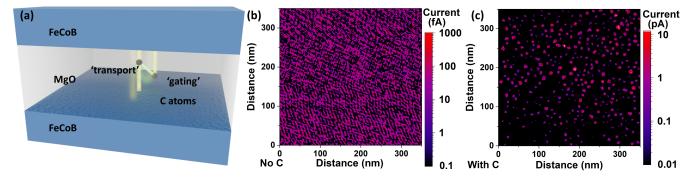


Figure 1. Atomic nanotransport paths. (a) Schematic of a nanotransport path formed by a 'transport' C atom that bridges the two electrodes of a microscale magnetic tunnel junction. A partly bridged path to a 'gating' C atom is also shown. Capacitive coupling and quantum interference effects are denoted by the green wiggle between the two atoms. Conducting tip Atomic Force Microscopy (AFM) scans of a half-MTJ sample (b) without C atoms in MgO and (c) with C atoms in MgO 0.9 nm away from the lower MgO interface. The interference patterns in panel (b) are due to noise at the background limit. The ~10nm nanotransport lateral size in panel (c) is the result of tip convolution.

detected by the tip. Assuming Gaussian noise, the standard deviation of the measured current is $\sigma \approx 0.065$ pA. Upon inserting C into MgO, we observe a series of current hotspots up to 120 pA that statistically contribute to the tail of the current distribution³⁴. The ~10 nm apparent lateral size is due to tip convolution over the several-atom-wide effective zone^{18,33} of the nanotransport path²⁸. Since quantum mechanical tunneling scales exponentially with the barrier's spatial width and energy height, the most prominent hotspot will funnel all the current across a microscale tunnel junction²⁸, as schematized in Fig. 1(a). It is this mechanism that enables atom-level properties in microelectronics here.

II. ATOM-LEVEL INFORMATION ENCODING IN A MICROSCALE DEVICE

Within a MgO MTJ (see Methods), the C-borne spin states can be electrically manipulated to encode information. The cyclical IV traces in Fig. 2(a) show two ON and OFF current branches that are linked through 'writing' events E_- and E_+ . Below these writing thresholds, the differential conductance $(\mathrm{d}I/\mathrm{d}V;\mathrm{panel}\ (\mathrm{b}))$ exhibits a set of two peaks whose bias positions rigidly shift by $\Delta_W \approx 70$ mV between the ON and OFF branches. Carefully crafted bias sweeps (panels (c-f)) below or above a writing threshold reveal how the writing event causes the conductance peak presence to change. As discussed in SI Note 4, the constant voltage gap $\Delta_{CG} = 310$ mV between the pair of conductance peaks can be tracked across several other junction states. Note how the current increases exponentially within this voltage gap.

These features are absent in MgO MTJs without C, i.e. when the nanotransport path only involves oxygen vacancies 27,29,33 . Also, while ${\rm O}^{2-}$ electromigration across transition metal oxides can explain resistive switching 35 , the ionic nature of MgO and low electric fields here preclude 36,37 this explanation for the writing events. We

therefore attribute these conductance peaks to the edges of the Coulomb blockade regime across the MgO MTJ thanks to electronic states of C atoms in the MgO barrier. Then, the writing-induced energy shift of the Coulomb gap may be due to charging environmental 'gating' C atoms that do not participate in transport, but are capacitively coupled to the 'transport' C atoms (see Fig. 1(a)) and essentially act as an electrostatic gate. This is supported in Fig. 2(a) by the presence of noisy regions EA1 and EA2 (semi-transparent datapoints). Indeed, the spectral position and width of these regions do not correspond to Coulomb blockade peaks in the present dataset, but rather in other datasets acquired on the same junction but with different 'transport' and 'gating' attributions of the C atoms upon thermal cycling. See SI Note 4 for details.

Within an appropriate capacitance model (see SI Note 5), the Coulomb gap $\Delta_{CG}=310$ mV indicates a 0.2 nm radius for the transport quantum dot: transport is proceeding across the electronic states of an individual carbon atom. Furthermore, if the voltage shift $\Delta_W \approx 70$ mV between junction states corresponds to changing the 'gating' atom's charge by 1 electron, then we infer that it is positioned at twice the radius away from the 'transport' C atom (see SI Note 5).

A similar hysteretic behavior induced by conductance jumps has been reported in model junctions^{38–44}, including abrupt switching between two conductance branches due to electron charging⁴¹. Inspired by this literature, we present in Fig. 2(h) the schematic of a two-quantum dot model that can explain this memristive Coulomb blockade behavior in our microjunction. The upper 'transport' quantum dot (TQD) is connected to both leads, while the lower 'gating' quantum dot (GQD) is connected only to the left lead. Both quantum dots are capacitively coupled together.

Starting at V=0 in the ON branch, the lower-lying levels of the TDQ are filled, the upper-lying are empty, and the single level of the GDQ is empty (see Fig. 2(h)1).

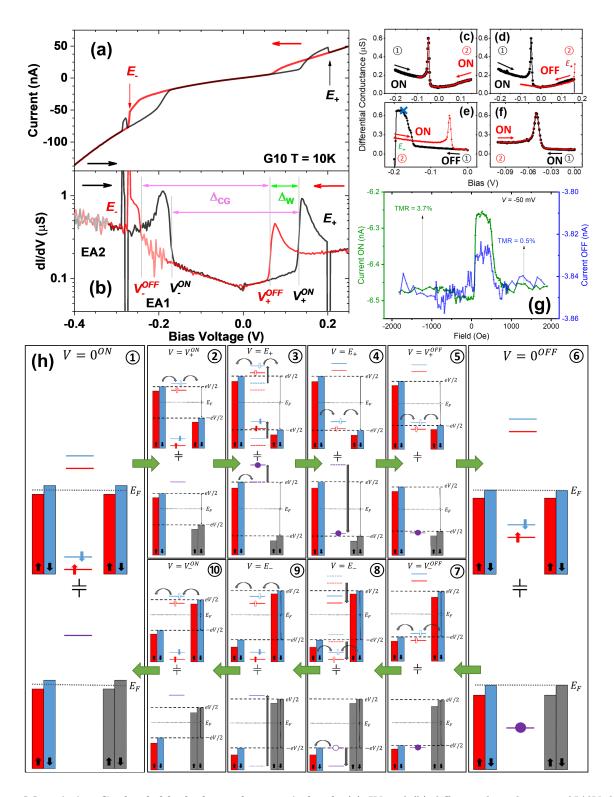


Figure 2. Memristive Coulomb blockade at the atomic level. (a) IV and (b) differential conductance $\mathrm{d}I/\mathrm{d}V$ data at T=10 K on junction G10. The E_+ and E_- writing events cause a shift $\Delta_W=73$ mV in the otherwise constant energy gap $\Delta_{CG}=310$ mV between conductance peaks. Transport noise due to interference with an environmental 'gating' atom are shown using semi-transparent datapoints. (c-f) $\mathrm{d}I/\mathrm{d}V$ data upon sweeping bias to test the interplay between the presence of the Coulomb blockade peak and the writing events E_- and E_+ . Starting in the black-coded junction state, bias is swept (black data of branch 1), and then reversed (red data of branch 2). Reaching a writing event while in the black state impacts the presence of the conductance peak. The blue cross in panel (e) pinpoints the bias and junction state in which the data of Fig. 3(a) was acquired. (g) Magnetoresistance traces at V=-50 mV in the ON/OFF junction states. (h) Model of a memristive Coulomb blockade involving at least one atom in the transport path, and at least one environmental 'gating' atom that is capacitively linked to the transport atom but doesn't participate directly in electronic transport across the junction (see also Fig 1(a)). The various operations of the memristive cycle, showing how charging/discharging the gating atom controls the energy levels of the transport atom, are shown.

At $V = V_{+}^{ON}$ (panel 2), sequential tunneling from the left lead onto the upper level of the TDQ occurs, leading to the conductance peak. Increasing the voltage to $V = E_{+}$ causes potential alignment with the GDQ level (panel 3). Electronic charging from the left electrode makes the levels of both QDs rise (step 1): the TQD's higher levels are above the potential, while the lower levels lie between the potential window offered by the electrodes. After equilibration, electron escape from the TQD occurs, and sequential tunneling starts through the lower levels. Within a narrow energy window, either the system trivially returns from 3 to 2, or the new dynamic filling of the TQD's energy levels capacitively lowers the GDQ's level (see Fig. 2(h)4). This capacitive back-action traps the electron that filled the GDQ level, preventing it from jumping back onto the electrode. This causes a conductance jump from the ON to OFF branch, and only a negative potential can release this trapped electron and revert the junction back to the ON state.

If the voltage is now decreased to V_{+}^{OFF} (see Fig. 2(h)5), another conductance peak is observed due to sequential tunneling through the lower lying level of the TQD. Then, at V=0 (see Fig. 2(h)6), the Coulomb blockade region is recovered but in an energy window that is shifted by the presence of the electron on the GDQ.

Similar arguments can describe the process of electron escape from the GDQ and the switch from the OFF back to the ON transport regime (see panels 7-10 of Fig. 2(h)). This two-QD capacitive charging cycle, which describes the experimental data of Fig. 2(b), can also be adjusted for other cases. The examples of Fig. 2(d) and SI Fig. S4 are fulfilled if the upper levels of the TQD lie below the empty level of the GDQ in the ON state. Then, an electron tunneling from the left electrode would address the GDQ level around $V=E_-$ before reaching the edge of the Coulomb blockade region.

III. QUANTUM INTERFERENCE EFFECTS

The discrete energy levels of the transport and gating quantum dots give rise to quantum transport interference effects. We present in Fig. 3(a) the temperature dependence of the current measured on junction G10 at V=-170 mV. As emphasized by the blue cross in Fig. 2(e), the junction is bistable at 10 K at this bias. Upon cooling down from 140 K, the current broadens into two ON/OFF branches, with intermediate spectral weight of low intensity (MID branch). Further evidence of these regimes appears in SI Note 7. Since temperature alone can promote a dominant transport branch, we conclude that electron-phonon interactions, *i.e.* vibrons, are also involved in quantum interference transport here, in line with prior literature $^{45-48}$.

We use bias-dependent current statistics to observe transport branches due to quantum interference. We first plot in Fig. 3(b) differential conductance data of junction C5 at T=10 K. On the log scale, we observe sizable in-

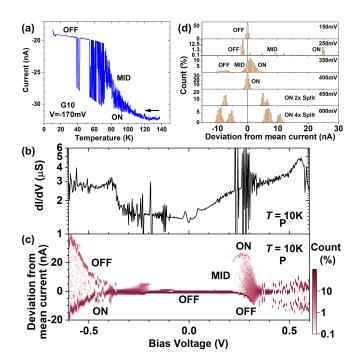


Figure 3. Quantum transport interference between individual carbon atoms. (a) Intensity as function of temperature at -2000 Oe and -170 mV for junction G10. (b-d): junction C5. (b) Differential conductance at 10 K for the P magnetic state. (c) Color map of the statistic weight of the current deviation from the mean current as a function of applied bias. The junction P magnetic state was used. At each bias value, 1000 current measurements were acquired. Datasets at select voltage values are shown in panel (d).

creases in conductance, and the clear appearance of noise for V < -0.4 V and for V > 0.3 V. Within -0.6 < V(V) < +0.6, after setting the dc applied bias, we measured the current 1000 times. The statistics of a given current deviation from the mean current as a function of applied bias are plotted in panel (c). Within |V| < 0.2V, the current remains essentially stable along the OFF branch. For |V| > 0.2 V, the transition to the MID state can appear. This is especially visible within 0.2 < V(V) < 0.4. While the OFF branch shifts to values below the mean, the MID branch collapses into the dominant branch around V = 0.4 V. A higher resolution dataset is shown in SI Note 1. For V > 0.4 V, this branch splits into two ON/OFF branches. A similar branching is seen for V < -0.4 V. Erratically, each of these two branches can split into two subbranches, for a total of four branches (see Fig. 3(d)). The conductance noise (panel c) thus arises from transport interference between these branches which are visualized by our current statistics.

Overall, these experimental findings support a picture of vibron-mediated co-tunneling and/or Coulomb drag between nanotransport paths⁵ due to blockade effects such as Franck-Condon blockade⁴⁵. According to the theory of out-of-equilibrium polaron dynamics^{47,49}, transport across an impurity with discrete energy levels, such

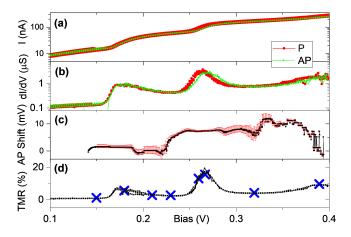


Figure 4. Spin accumulation due to Pauli spin blockade. (a) Current-voltage characteristic for the P and AP junction states, and (b) the resulting $\mathrm{d}I/\mathrm{d}V$ differential conductance. (c) Voltage shift between the P and AP conductance data (see Methods for details). (d) Bias dependence of the tunnel magnetoresistance (TMR) calculated from (a). Blue crosses indicate TMR amplitudes obtained from I(H) experiments. All data: junction G10.

as a quantum dot or a molecular orbital that is strongly coupled to a vibrational degree of freedom and that is tunnel coupled to two leads, can explain the observed multi-stability of different states and the telegraphic switching between the different intensity branches. The bias voltage acts as an effective temperature and a force that modulates the oscillator potential. Around specific voltage biases, the effective vibron energy potential landscape develops several minima, and thus promotes metastability between different occupation states. Two scenarios are possible. 1) Thermally activated switching between different intensity branches related to each of the well-separated potential minima can occur¹⁰. 2) Large fluctuations around a single intensity branch occur when at least two minima are sufficiently degenerate to energetically trigger an interference effect 50,51 . In this latter case, intermediate states outside the well minima are measured.

IV. SPINTRONIC SIGNATURES

The memristive behavior of the Coulomb blockade peak due to environmental charging represents one level of information encoding, with a write success rate > 80% (see SI Note 3). To examine how the spin polarization of the charge current impacts the atom-level memristive Coulomb blockade effect and quantum interference effects, we compare transport properties upon switching the orientation of the electrodes' magnetization from parallel (P) to antiparallel (AP). Note that C atoms in MgO are paramagnetic, *i.e.* can bear an unpaired spin¹⁸.

We plot in Fig. 4(a) the IV in the MTJ's P and AP states at T=10 K. Both exhibit a series of plateaus

and increases that are absent in junctions without C atoms^{27–29}. The corresponding differential conductance $(\mathrm{d}I/\mathrm{d}V)$ data (see panel (b)) reveals a series of peaks. While the P and AP datasets share similar traits, the AP plot appears to shift to higher bias as the onset of each conductance increase is reached. This is confirmed through an analysis of the correlated shift between the two datasets in Fig. 4(c) (see Methods).

The tunnel magnetoresistance TMR = $\frac{I_P}{I_{AP}-1}$ characterizes to what extent the two spin channels of current flowing across the device are asymmetric. In our MgO MTJs without C²⁷, we observe TMR $\approx 200~\%$ at 10 K around V=0, and a mostly monotonous TMR decreasing with increasing |V|. When C atoms are introduced into MgO, we observe only a few % TMR around V=0. Instead, due to the shift in AP conductance to higher bias with each succeeding conductance peak, the TMR bias dependence closely mimics the junction conductance (compare panels (b) and (d) of Fig. 4). This unusual, highly structured TMR bias dependence 16 is confirmed through discrete I(H) datasets at fixed V (crosses in Fig. 4(d)). We observe local TMR maxima precisely on the conductance peaks, with an absolute maximum of 15%.

We present I(H) data in Fig. 2(g) in both the ON and OFF states of the junction, taken at V=-50 mV; *i.e.* precisely at the bias value corresponding to the memristive Coulomb blockade peak shown in panels (c-e) of Fig. 2. We observe that I_P increases and that I_P - I_{AP} is multiplied by 7, so that the TMR increases from 0.5% in the OFF state to 3.7% in the ON state due to the Coulomb blockade peak. Within the paradigm of MgO tunneling spintronics⁵², this suggests that overcoming the Coulomb blockade effectively opens an additional transport channel for the dominant majority spin carriers.

According to Płomińska and Weymann⁵³, the similar bias-dependent conductance peaks in the P and AP datasets, which yield a similar TMR trace, is the signature of a special kind of Coulomb blockade involving the Pauli exclusion principle called Pauli Spin blockade 54-56. As the electronic level of the TQD is reached with applied bias, sequential tunneling is suppressed while cotunneling mechanisms become dominant and modify the TQD's spin state (and eventually its charge¹⁸) as a form of spintronic anisotropy^{57–59}. With increasing voltage, the FeCoB/MgO tunneling-induced accumulation of mostly spin up carriers lifts the spin state degeneracy. This spin splitting differs between the MTJ's P and AP states due to different energy alignments of the C electronic levels^{18,53}. This effect is also modeled by our schematic in Fig 2(h), which features this spin splitting. In the P state, the potential of the electrodes will align with the spin-split energy levels of the TQD at lower absolute bias than in the AP state. This would result in a voltage shift between the conductance peaks. SI Notes 1 and 4 provide additional evidence of this effect.

The conductance shift of Fig. 4(c) is thus an exper-

imental manifestation of spin accumulation. Spin accumulation explains the shift in quantum interference data and the spin polarization of the transport branch therein (see SI Notes 1-2). It also explains why the TMR bias dependence tracks that of junction conductance (see Fig. 4(d)), as well as the huge increase in I_{P} - I_{AP} due to the memristive Coulomb peak (see Fig. 2(g)) leading to the seven-fold TMR enhancement. The best qualitative agreement between the results of Płomińska and Weymann 53 and our experimental datasets is that of 'parallel' or 'T-shaped' electronic transport across spin states, rather than the other series scenario proposed. This supports the atomic description of the effective nanotransport path across our microscale MTJs.

To obtain more insight into the origin of the magnetic field experienced by the transport C atom, we performed nitrogen vacancy (NV) center microscopy experiments on a half-MTJ sample (see Methods), and simulated these data using Mumax3^{60,61} to extract micromagnetic parameters. An example of experimental data and simulation is shown in Fig. 5(a) for a NV center height of 90 nm. Using the same parameters, we are able to fit other NV scans at heights ranging from 60 nm to 180 nm. This allows us to confidently extrapolate the stray field at 2.5 nm above the ferromagnetic surface. Figs. 5(b) (left/right) show the extrapolated maps of the longitudinal $B_{||}$ / transverse B_{\perp} components of the stray field⁶². We find that no field component exceeds 20 mT, *i.e.* or-

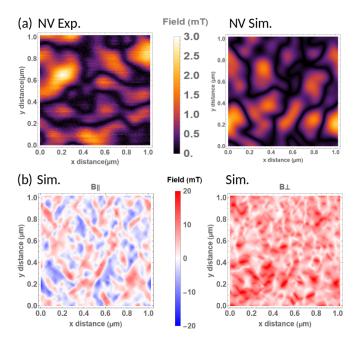


Figure 5. Magnetic stray field on the C atom due to the ferromagnetic electrode. (a) NV center magnetometry scan 90 nm away from the half-MTJ sample surface. The color encodes the stray field absolute value projected onto the NV center axis (100-oriented diamond tip). (b) Extrapolated maps of the stray field longitudinal $B_{||}$ and transverse B_{\perp} components.

ders of magnitude below values inferred by the spintronic energy shifts observed in magnetotransport (see Fig. 4). We thus infer that the effect arises from the electronic magnetic field ~ 50 T due to spin-polarized charge transfer from the ferromagnetic metal, in combination with bias-induced spintronic anisotropy¹⁸.

V. CONCLUSION

To conclude, inserting C atoms into ultrathin MgO layers generates localized paramagnetic 18 states. Experiments on micronic FeCoB/MgO/FeCoB magnetic tunnel junctions, which are crafted using straightforward technological processes, show that the effective nanotransport path²⁸ involves individual C atoms. Their discrete energy levels promote Coulomb blockade effects that can be reproducibly shifted in energy by charging events on a neighboring C atom. The tunnel coupling between these transport and environmental 'gating' carbon atoms promotes quantum interference effects. Spin-polarized transport induces spin accumulation that further lifts the spin degeneracy of the unpaired C electron in MgO. This leads to a voltage shift in Coulomb peaks between the MTJ's P and AP datasets, and to quantum interference effects. Spin accumulation also accounts for the huge enhancement of the spintronic performance when a Coulomb peak is memristively controlled.

We thus demonstrate how to use both the electron charge and spin to encode information on an individual paramagnetic atom in a solid-state, industrializable device. These results showcase MgO tunneling spintronics as a promising industrial platform for quantum technologies at potentially practical temperatures, to deploy quantum transport effects that are normally only seen in model junctions. Naturally, compared to research on model junctions, the main difficulty here will be to engineer the C-borne paths embedded into the MTJ pillar so as to obtain 1) a higher device-to-device reproducibility at 2) with electronic stability at higher temperatures. Possible approaches include engineering the impedances that electronically link the transport and gating atoms to the magnetic tunnel junction electrodes; engineering the paramagnetic center's chemical bonds to MgO; and controlling the density of oxygen vacancies³³. Final applications of quantum spintronics not only encompass information encoding¹⁷, but also energy harvesting^{18,19,63} vectors.

VI. METHODS

A. Stack growth and MTJ processing

 $\begin{array}{l} Glass//Ta(5)/Co(10)/IrMn(7.5)/CoFeB(4) \\ /MgO(0.9)/C(0.6)MgO(1.7)/CoFeB(3)/Ta(2)/Pt(1) \\ samples \ (all\ thicknesses\ in\ nm)\ were\ sputter-grown\ on \end{array}$

Corning 1737 glass substrates⁶⁴. Stacks were postannealed in an in-plane magnetic field of 200 Oe for one hour at a temperature T_a of 200 °C to magnetically pin the lower electrode thanks to the IrMn antiferromagnetic layer. Samples were then processed by optical lithography 65 into 20 μ m-diameter MTJs, and measured on a variable-temperature magnetotransport bench. 54 junctions were tested on these samples, 35 of them were either metallic of open circuit. Among the other 19 interesting junctions, all the reported effects have been observed in several of them. 8 of them presented memristive properties with branch jumps and conductance peaks, among which at least 3 presented magnetomemristive properties correlating with the conductance, while 7 of them presented jumps and noisy behaviors typical of interferences between several nanotransport paths (see SI Note 6).

B. Conducting tip atomic force microscopy

Local probe experiments were carried out on a $\mathrm{Si//Ta(3)/Pt(5)/IrMn(8)/CoFeB(5)/MgO(0.4)/C(0.6)}$ /MgO(0.6) stack using an Icon AFM (Atomic Force Microscope) from Bruker. Topography images were acquired in standard contact mode (force constant) and, simultaneously, using an additional TUNA module (Bruker), which allowed current collection via a conductive tip. A voltage bias of 10 mV was applied to conductive AFM tips (Bruker SCM-PIT-V2; PtIr-coated Si with a 3N/m elastic constant) to enable electron collection. The current amplifier gain was set to 10 pA/V.

C. NV center scanning magnetometry

We conducted NV scanning magnetometry using a Qzabre microscope, which integrates scanned probe microscopy and optically detected magnetic resonance. This enabled us to image the magfield distribution induced by the magnetic netic of the ferromagnetic bottom electrode. texture The electrode stack configuration is as follows: Glass/Ta(5)/Co(10)/IrMn(7.5)/CoFeB(4)/MgO(2.5)/Pt(2.5). For this study, we employed a commercial Qzabre tip (QST-100). Scans were carried out at four different heights: 180 nm, 130 nm, 90 nm, and 60 nm. Below 60 nm, the image quality deteriorated, likely due to a fluorescence quenching effect. To simulate the stray field, we used the mumax3 code^{60,61}, incorporating a random spatial distribution of anisotropy direction with 50 nm magnetic grains. Our mumax3 problem will be made available upon request. Further details will be provided in a more technical paper.

D. Voltage shift calculation

The voltage shift between the P and AP conductance data of Fig. 4(c) was calculated by doing a curve fitting of AP data over P data using a rolling window of 40mV width, with the voltage shift as the only parameter. The fit and estimation of uncertainties were done using the LMFIT python module⁶⁶ (Non-Linear Least-Squares Minimization and Curve-Fitting). The calculated voltage shift was then defined as the voltage shift of the mean bias value within the rolling window.

VII. ACKNOWLEDGEMENTS

We gratefully acknowledge PhD funding for M.L. from Ecole Polytechnique. We acknowledge financial support from the ANR (ANR-21-CE50-0039), the Contrat de Plan Etat-Region grants in 2006 and 2008, by "NanoTérahertz", a project co-funded by the ERDF 2014–2020 in Alsace (European Union fund) and by the Region Grand Est through its FRCR call, by the impact project LUE-N4S part of the French PIA project "Lorraine Université d'Excellence", reference ANR-15IDEX-04-LUE and by the FEDER-FSE "Lorraine et Massif Vosges 2014–2020", a European Union Program. This work of the Interdisciplinary Thematic Institute QMat, as part of the ITI 2021-2028 program of the University of Strasbourg, CNRS and Inserm, was supported by IdEx Unistra (ANR 10 IDEX 0002), and by SFRI STRAT'US project (ANR 20 SFRI 0012) and EUR QMAT ANR-17-EURE-0024 under the framework of the French Investments for the Future Program. This work was supported by France 2030 government investment plan under grant reference PEPR SPIN-MAT ANR-22-EXSP-0007 and PEPR SPIN -ADAGE ANR-22-EXSP-0006.

REFERENCES

- ¹T. Li, V. K. Bandari, and O. G. Schmidt, "Molecular electronics: Creating and bridging molecular junctions and promoting its commercialization," Advanced Materials **35** (2023), 10.1002/adma.202209088.
- ²R. L. McCreery, "Carbon-based molecular junctions for practical molecular electronics," Accounts of Chemical Research 55, 2766–2779 (2022).
- ³W. Peng, H. Wang, H. Lu, L. Yin, Y. Wang, B. Grandidier, D. Yang, and X. Pi, "Recent progress on the scanning tunneling microscopy and spectroscopy study of semiconductor heterojunctions," Small 17 (2021), 10.1002/smll.202100655.
- ⁴D. A. Ryndyk, "Electron-Electron Interaction and Coulomb Blockade," in *Theory of Quantum Transport at Nanoscale*, Vol. 184 (Springer International Publishing, Cham, 2016) pp. 123–147.
- ⁵A. Keller, J. Lim, D. Sánchez, R. López, S. Amasha, J. Katine, H. Shtrikman, and D. Goldhaber-Gordon, "Cotunneling Drag Effect in Coulomb-Coupled Quantum Dots," Physical Review Letters 117 (2016), 10.1103/PhysRevLett.117.066602.
- ⁶E. Burzuri, Y. Yamamoto, M. Warnock, X. Zhong, K. Park, A. Cornia, and H. S. J. van der Zant, "Franck-condon blockade in a single-molecule transistor," 14, 3191–3196 (2014).

- ⁷M. Ganzhorn, S. Klyatskaya, M. Ruben, and W. Wernsdorfer, "Strong spin–phonon coupling between a single-molecule magnet and a carbon nanotube nanoelectromechanical system," 8, 165– 169 (2013).
- ⁸J. J. Parks, A. R. Champagne, T. A. Costi, W. W. Shum, A. N. Pasupathy, E. Neuscamman, S. Flores-Torres, P. S. Cornaglia, A. A. Aligia, C. A. Balseiro, G. K.-L. Chan, H. D. Abruña, and D. C. Ralph, "Mechanical control of spin states in spin-1 molecules and the underscreened kondo effect," 328, 1370–1373 (2010).
- ⁹T. Miyamachi, M. Gruber, V. Davesne, M. Bowen, S. Boukari, L. Joly, F. Scheurer, G. Rogez, T. K. Yamada, P. Ohresser, E. Beaurepaire, and W. Wulfhekel, "Robust spin crossover and memristance across a single molecule," Nature Communications 3, 938 (2012).
- ¹⁰S. J. van der Molen and P. Liljeroth, "Charge transport through molecular switches," **22**, 133001 (2010).
- ¹¹D. Secker, S. Wagner, S. Ballmann, R. Härtle, M. Thoss, and H. B. Weber, "Resonant Vibrations, Peak Broadening, and Noise in Single Molecule Contacts: The Nature of the First Conductance Peak," Physical Review Letters 106 (2011), 10.1103/Phys-RevLett.106.136807.
- ¹²Y.-J. Zeng, D. Wu, X.-H. Cao, Y.-X. Feng, L.-M. Tang, and K.-Q. Chen, "Significantly enhanced thermoelectric performance of molecular junctions by the twist angle dependent phonon interference effect," 8, 11884–11891 (2020).
- ¹³ J. E. Greenwald, J. Cameron, N. J. Findlay, T. Fu, S. Gunasekaran, P. J. Skabara, and L. Venkataraman, "Highly non-linear transport across single-molecule junctions via destructive quantum interference," 16, 313–317 (2020).
- ¹⁴L. D. N. Mouafo, F. Godel, G. Melinte, S. Hajjar-Garreau, H. Majjad, B. Dlubak, O. Ersen, B. Doudin, L. Simon, P. Seneor, and J.-F. Dayen, "Anisotropic Magneto-Coulomb Properties of 2D-0D Heterostructure Single Electron Device," Advanced Materials 30, 1802478 (2018).
- ¹⁵J. Escolar, N. Peimyoo, M. F. Craciun, H. A. Fernandez, S. Russo, M. D. Barnes, and F. Withers, "Anisotropic magnetoconductance and Coulomb blockade in defect engineered \${\mathrm{Cr}}_{2}{\mathrm{Ge}}_{2}{\mathrm{Te}}_{6}\$ van der Waals heterostructures," Physical Review B 100, 054420 (2019).
- ¹⁶R. Suzuki, Y. Tadano, L. D. Anh, M. Tanaka, and S. Ohya, "Unconventional bias dependence of tunnel magnetoresistance induced by the Coulomb blockade effect," AIP Advances 11, 125029 (2021).
- ¹⁷K. Katcko, E. Urbain, F. Ngassam, L. Kandpal, B. Chowrira, F. Schleicher, U. Halisdemir, D. Wang, T. Scherer, D. Mertz, B. Leconte, N. Beyer, D. Spor, P. Panissod, A. Boulard, J. Arabski, C. Kieber, E. Sternitzky, V. Da Costa, M. Hehn, F. Montaigne, A. Bahouka, W. Weber, E. Beaurepaire, C. Kübel, D. Lacour, M. Alouani, S. Boukari, and M. Bowen, "Encoding Information on the Excited State of a Molecular Spin Chain," Advanced Functional Materials 31, 2009467 (2021).
- ¹⁸K. Katcko, E. Urbain, B. Taudul, F. Schleicher, J. Arabski, E. Beaurepaire, B. Vileno, D. Spor, W. Weber, D. Lacour, S. Boukari, M. Hehn, M. Alouani, J. Fransson, and M. Bowen, "Spin-driven electrical power generation at room temperature," Communications Physics 2 (2019), 10.1038/s42005-019-0207-8.
- ¹⁹B. Chowrira, L. Kandpal, M. Lamblin, F. Ngassam, C. Kouakou, T. Zafar, D. Mertz, B. Vileno, C. Kieber, G. Versini, B. Gobaut, L. Joly, T. Ferté, E. Monteblanco, A. Bahouka, R. Bernard, S. Mohapatra, H. Prima Garcia, S. Elidrissi, M. Gavara, E. Sternitzky, V. Da Costa, M. Hehn, F. Montaigne, F. Choueikani, P. Ohresser, D. Lacour, W. Weber, S. Boukari, M. Alouani, and M. Bowen, "Quantum advantage in a molecular spintronic engine that harvests thermal fluctuation energy," Advanced Materials 34 (2022), 10.1002/adma.202206688.
- ²⁰C. Barraud, K. Bouzehouane, C. Deranlot, D. J. Kim, R. Rakshit, S. Shi, J. Arabski, M. Bowen, E. Beaurepaire, S. Boukari, F. Petroff, P. Seneor, and R. Mattana, "Phthalocyanine based

- molecular spintronic devices," Dalton Transactions 45, 16694–16699 (2016).
- ²¹M. Bowen, J.-L. Maurice, A. Barthélémy, P. Prod'homme, E. Jacquet, J.-P. Contour, D. Imhoff, and C. Colliex, "Biascrafted magnetic tunnel junctions with bistable spin-dependent states," Applied Physics Letters 89, 103517 (2006).
- ²²A. D. Kent and D. C. Worledge, "A new spin on magnetic memories," Nature Nanotechnology 10, 187–191 (2015).
- ²³ J. Torrejon, M. Riou, F. A. Araujo, S. Tsunegi, G. Khalsa, D. Querlioz, P. Bortolotti, V. Cros, K. Yakushiji, A. Fukushima, H. Kubota, S. Yuasa, M. D. Stiles, and J. Grollier, "Neuromorphic computing with nanoscale spintronic oscillators," Nature 547, 428–431 (2017).
- ²⁴L. Zhang, B. Fang, J. Cai, M. Carpentieri, V. Puliafito, F. Garesci, P. K. Amiri, G. Finocchio, and Z. Zeng, "Ultrahigh detection sensitivity exceeding 10 ⁵ V/W in spin-torque diode," Applied Physics Letters 113, 102401 (2018).
- ²⁵P. P. Freitas, R. Ferreira, S. Cardoso, and F. Cardoso, "Magnetoresistive sensors," Journal of Physics-Condensed Matter 19 (2007), 10.1088/0953-8984/19/16/165221.
- ²⁶Y. Lu, M. Tran, H. Jaffrès, P. Seneor, C. Deranlot, F. Petroff, J.-M. George, B. Lépine, S. Ababou, and G. Jézéquel, "Spin-Polarized Inelastic Tunneling through Insulating Barriers," Physical Review Letters 102, 176801 (2009).
- ²⁷F. Schleicher, U. Halisdemir, D. Lacour, M. Gallart, S. Boukari, G. Schmerber, V. Davesne, P. Panissod, D. Halley, H. Majjad, Y. Henry, B. Leconte, A. Boulard, D. Spor, N. Beyer, C. Kieber, E. Sternitzky, O. Cregut, M. Ziegler, F. Montaigne, E. Beaurepaire, P. Gilliot, M. Hehn, and M. Bowen, "Localized states in advanced dielectrics from the vantage of spin- and symmetry-polarized tunnelling across MgO," Nature Communications 5 (2014), 10.1038/ncomms5547.
- ²⁸M. Studniarek, U. Halisdemir, F. Schleicher, B. Taudul, E. Urbain, S. Boukari, M. Hervé, C.-H. Lambert, A. Hamadeh, S. Petit-Watelot, O. Zill, D. Lacour, L. Joly, F. Scheurer, G. Schmerber, V. D. Costa, A. Dixit, P. A. Guitard, M. Acosta, F. Leduc, F. Choueikani, E. Otero, W. Wulfhekel, F. Montaigne, E. N. Monteblanco, J. Arabski, P. Ohresser, E. Beaurepaire, W. Weber, M. Alouani, M. Hehn, and M. Bowen, "Probing a device's active atoms," Advanced Materials 29, 1606578 (2017).
- ²⁹F. Schleicher, B. Taudul, U. Halisdemir, K. Katcko, E. Monteblanco, D. Lacour, S. Boukari, F. Montaigne, E. Urbain, L. M. Kandpal, J. Arabski, W. Weber, E. Beaurepaire, M. Hehn, M. Alouani, and M. Bowen, "Consolidated picture of tunnelling spintronics across oxygen vacancy states in MgO," Journal of Physics D: Applied Physics 52, 305302 (2019).
- ³⁰L. M. Kandpal, B. Taudul, E. Monteblanco, A. Kumar, K. Katcko, F. Schleicher, P. Gupta, S. Boukari, W. Weber, V. Da Costa, J. D. Costa, T. Böhnert, R. Ferreira, P. Freitas, M. Hehn, M. Alouani, P. K. Muduli, D. Lacour, and M. Bowen, "Oxygen vacancy-driven spin-transfer torque across MgO magnetic tunnel junctions," npj Spintronics 3, 1–7 (2025).
- ³¹D. J. Kim, W. S. Choi, F. Schleicher, R. H. Shin, S. Boukari, V. Davesne, C. Kieber, J. Arabski, G. Schmerber, E. Beaurepaire, W. Jo, and M. Bowen, "Control of defect-mediated tunneling barrier heights in ultrathin MgO films," Applied Physics Letters 97, 263502 (2010).
- ³²F. Schleicher, U. Halisdemir, E. Urbain, D. Lacour, M. Gallart, S. Boukari, F. Montaigne, E. Beaurepaire, P. Gilliot, M. Hehn, and M. Bowen, "MgO magnetic tunnel junctions of enduring F-type upon annealing," Journal of Physics D: Applied Physics 48, 435004 (2015).
- ³³B. Taudul, E. N. Monteblanco, U. Halisdemir, D. Lacour, F. Schleicher, F. Montaigne, E. Beaurepaire, S. Boukari, M. Hehn, M. Alouani, and M. Bowen, "Tunneling Spintronics across MgO Driven by Double Oxygen Vacancies," Advanced Electronic Materials 3, 1600390 (2017).
- ³⁴V. Da Costa, C. Tiusan, T. Dimopoulos, and K. Ounadjela, "Tunneling phenomena as a probe to investigate atomic scale fluctuations in metal/oxide/metal magnetic tunnel junctions," Physical

Review Letters 85, 876-879 (2000).

³⁵I. Hwang, M.-J. Lee, G.-H. Buh, J. Bae, J. Choi, J.-S. Kim, S. Hong, Y. S. Kim, I.-S. Byun, S.-W. Lee, S.-E. Ahn, B. S. Kang, S.-O. Kang, and B. H. Park, "Resistive switching transition induced by a voltage pulse in a Pt/NiO/Pt structure," Applied Physics Letters 97, 052106 (2010).

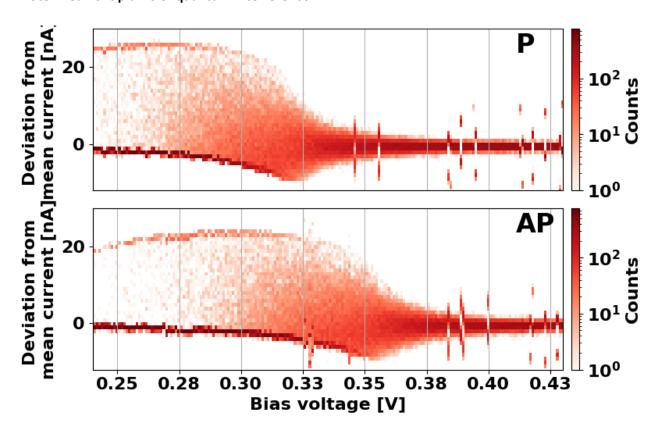
³⁶E. Bertin, D. Halley, Y. Henry, N. Najjari, H. Majjad, M. Bowen, V. DaCosta, J. Arabski, and B. Doudin, "Random barrier doublewell model for resistive switching in tunnel barriers," Journal of Applied Physics 109, 083712 (2011).

- ³⁷J. M. Aguiar-Hualde and M. Alouani, "Taming the resistive switching in Fe/MgO/V/Fe magnetic tunnel junctions: An ab initio study," Journal of Magnetism and Magnetic Materials 372, 167-172 (2014).
- ³⁸C. Jia, A. Migliore, N. Xin, S. Huang, J. Wang, Q. Yang, S. Wang, H. Chen, D. Wang, B. Feng, Z. Liu, G. Zhang, D.-H. Qu, H. Tian, M. A. Ratner, H. Q. Xu, A. Nitzan, and X. Guo, "Covalently bonded single-molecule junctions with stable and reversible photoswitched conductivity," Science 352, 1443-1445 (2016).
- ³⁹E. Lörtscher, J. Ciszek, J. Tour, and H. Riel, "Reversible and controllable switching of a single-molecule junction," 2, 973–977 (2006)
- ⁴⁰F. Schwarz, G. Kastlunger, F. Lissel, C. Egler-Lucas, S. N. Semenov, K. Venkatesan, H. Berke, R. Stadler, and E. Lörtscher, "Field-induced conductance switching by charge-state alternation in organometallic single-molecule junctions," Nature Nanotechnology 11, 170-176 (2016).
- ⁴¹S. W. Wu, N. Ogawa, G. V. Nazin, and W. Ho, "Conductance Hysteresis and Switching in a Single-Molecule Junction," The Journal of Physical Chemistry C 112, 5241–5244 (2008).
- $^{\rm 42}{\rm T.}$ Leoni, O. Guillermet, H. Walch, V. Langlais, A. Scheuermann, J. Bonvoisin, and S. Gauthier, "Controlling the Charge State of a Single Redox Molecular Switch," Physical Review Letters 106 (2011), 10.1103/PhysRevLett.106.216103.
- ⁴³L. Gerhard, K. Edelmann, J. Homberg, M. Valášek, S. G. Bahoosh, M. Lukas, F. Pauly, M. Mayor, and W. Wulfhekel, "An electrically actuated molecular toggle switch," Nature Communications 8, 14672 (2017).
- ⁴⁴L. Zhang, T. Yang, W. Zhang, D. Qi, X. He, K. Xing, P. K. J. Wong, Y. P. Feng, and A. T. S. Wee, "Bi-stable electronic states of cobalt phthalocyanine molecules on two-dimensional vanadium diselenide," Applied Materials Today 18, 100535 (2020).
- $^{\rm 45}{\rm J}.$ Koch, F. von Oppen, and A. V. Andreev, "Theory of the Franck-Condon blockade regime," Physical Review B 74 (2006), 10.1103/PhysRevB.74.205438.
- ⁴⁶M. Galperin, M. A. Ratner, and A. Nitzan, "Molecular transport junctions: vibrational effects," Journal of Physics: Condensed Matter 19, 103201 (2007).
- ⁴⁷D. Mozyrsky, M. B. Hastings, and I. Martin, "Intermittent polaron dynamics: Born-Oppenheimer approximation out of equilibrium," Physical Review B 73 (2006), 10.1103/Phys-RevB.73.035104.
- $^{48}\mathrm{S.~V.}$ Aradhya and L. Venkataraman, "Single-molecule junctions beyond electronic transport," Nature Nanotechnology 8, 399–410
- ⁴⁹M. Galperin, M. A. Ratner, and A. Nitzan, "Hysteresis, Switching, and Negative Differential Resistance in Molecular Junctions:

- A Polaron Model," Nano Letters 5, 125–130 (2005).
- ⁵⁰M. Wierzbicki and R. Swirkowicz, "Influence of interference effects on thermoelectric properties of double quantum dots," Physical Review B 84 (2011), 10.1103/PhysRevB.84.075410.
- ⁵¹S. W. Wu, G. V. Nazin, X. Chen, X. H. Qiu, and W. Ho, "Control of Relative Tunneling Rates in Single Molecule Bipolar Electron Transport," Physical Review Letters 93 (2004), 10.1103/Phys-RevLett.93.236802.
- ⁵²J. S. Moodera, G.-X. Miao, and T. S. Santos, "Frontiers in spinpolarized tunneling," Physics Today 63, 46-51 (2010).
- ⁵³A. Płomińska and I. Weymann, "Magnetoresistive properties of a double magnetic molecule spin valve in different geometrical arrangements," Journal of Magnetism and Magnetic Materials **480**, 11–21 (2019).
- ⁵⁴J. Fransson and M. Råsander, "Pauli spin blockade in weakly coupled double quantum dots," Physical Review B 73 (2006), 10.1103/PhysRevB.73.205333.
- ⁵⁵D. M.-T. Kuo, S.-Y. Shiau, and Y.-c. Chang, "Theory of spin blockade, charge ratchet effect, and thermoelectrical behavior in serially coupled quantum dot system," Physical Review B 84 (2011), 10.1103/PhysRevB.84.245303.
- $^{56}\mathrm{A.}$ Płomińska and I. Weymann, "Pauli spin blockade in double molecular magnets," Physical Review B 94 (2016), 10.1103/PhysRevB.94.035422.
- ⁵⁷M. Misiorny, I. Weymann, and J. Barnaś, "Spin effects in transport through single-molecule magnets in the sequential and cotunneling regimes," Physical Review B 79, 224420 (2009).
- ⁵⁸M. Misiorny and I. Weymann, "Transverse anisotropy effects on spin-resolved transport through large-spin molecules," Physical Review B 90 (2014), 10.1103/PhysRevB.90.235409.
- ⁵⁹T. Saygun, J. Bylin, H. Hammar, and J. Fransson, "Voltage-Induced Switching Dynamics of a Coupled Spin Pair in a Molecular Junction," Nano Letters 16, 2824-2829 (2016).
- ⁶⁰J. Leliaert, B. Van de Wiele, A. Vansteenkiste, L. Laurson, G. Durin, L. Dupré, and B. Van Waevenberge, "Current-driven domain wall mobility in polycrystalline permalloy nanowires: A numerical study," Journal of Applied Physics 115, 233903 (2014).
- ⁶¹A. Vansteenkiste, J. Leliaert, M. Dvornik, M. Helsen, F. Garcia-Sanchez, and B. Van Waeyenberge, "The design and verification of Mumax3," AIP Advances 4, 107133 (2014).
- $^{62}\mathrm{L}.$ P. et al., in preparation.
- ⁶³M. Bowen, "Atom-level electronic physicists are needed to develop practical engines with a quantum advantage," npj Quantum Information 9, 25 (2023).
- ⁶⁴J. Bernos, M. Hehn, F. Montaigne, C. Tiusan, D. Lacour, M. Alnot, B. Negulescu, G. Lengaigne, E. Snoeck, and F. G. Aliev, "Impact of electron-electron interactions induced by disorder at interfaces on spin-dependent tunneling in Co-Fe-B/MgO/Co-Fe-B magnetic tunnel junctions," Physical Review B 82 (2010), 10.1103/PhysRevB.82.060405.
- $^{65}\mathrm{D.~Halley,~H.~Majjad,~M.~Bowen,~N.~Najjari,~Y.~Henry,~C.~Ulhaq-$ Bouillet, W. Weber, G. Bertoni, J. Verbeeck, and G. Van Tendeloo, "Electrical switching in Fe/Cr/MgO/Fe magnetic tunnel junctions," Applied Physics Letters 92, 212115 (2008).
- $^{66}\mbox{``Non-linear least-squares minimization}$ and curve-fitting," .

Supplementary Information

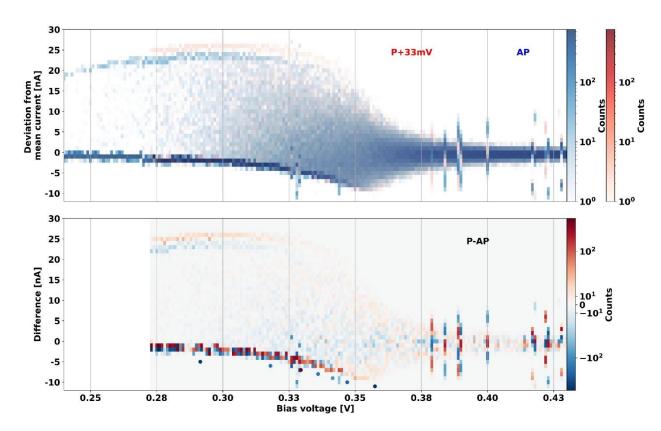
Note 1: Current plume of quantum interference



Suppl. Fig. S1: **Zoom on the plume of quantum interference.** Bias dependence of the frequency of the deviation from the mean current. Data at T = 10K in the MTJ's P (top) and AP (bottom) states is shown. Nanojunction C5 was used. Statistics are obtained on 800 points at each bias value.

We present in Suppl . Fig. S1 a high resolution dataset of the current distribution plume reported in Fig. 3 of the main text for the junction's P and AP states. We observe a positive 33mV bias shift of the AP dataset due to spin accumulation (see main text).

For each bias voltage we measured 800 times the junction current. The mean current is calculated and subtracted for all points inside the dataset, and finally an histogram is computed with a bin size of 1nA. The result of the histogram is represented on the Suppl . Fig. S1 by a vertical line of dots at the corresponding voltage bias, the color of a dot representing the number of counts in every bins of the histogram.

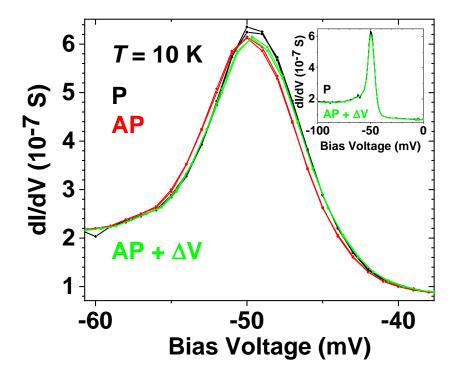


Suppl. Fig. S2: **Spintronic contrast in the plume of quantum interference.** (Top) Same data as in Suppl. Fig S. 1, but with a +33mV shift in the P data. (Bottom) Difference P-AP of the datasets of the top panel. The round dots below the lower branch represent an average of the lower branch difference data. They are centered around the range considered. These points are all blue-leaning: the lower branch is more strongly weighed in the MTJ's AP state.

To distinguish spintronic contrast, we overlap the datasets by manually removing the shift (see Fig. S2a). We note that the OFF branch (lower branch) overlaps rather well. On the other hand, the ON branch (upper branch) exhibits a different deviation from mean current in the MTJ's P and AP states. We attribute this differing deviation to a slight change in the effective potential landscape due to spin-polarized hybridization between the electrodes and the localized paramagnetic barrier states.

To further examine spintronic contrast, we then consider the difference P-AP between the datasets. The results are plotted in the bottom panel of Suppl. Fig. S2. We observe that the difference is very pronounced for the OFF branch. To confirm this trend, we're integrated this difference over several bias ranges. The position of the resulting round dots below the OFF branch represents the center of the range, while the color code shows the averaged result. Over the seven bias ranges considered, all averages of the OFF branch reveal that the OFF branch is more prevalent in the MTJ's AP state. We infer that the transport path responsible for the OFF branch is spin-polarized.

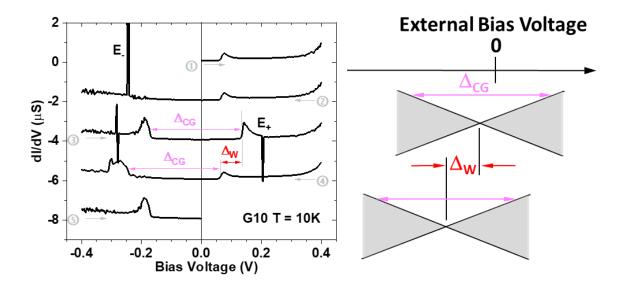
Note 2: Spin accumulation at negative bias



Suppl. Fig. S3: **Spin accumulation on the sharpest Coulomb blockade peak found at V<0.** Bias dependence of differential conductance dI/dV at T= 10K on junction G10 in the MTJ's P (black) and AP (red) states. the AP data in green was bias-shifted by +0.35mV. This shift enables a qualitatively good overlap of the conductance peak with that seen in the P data. Inset: Overview of the conductance peak in the MTJ's P state, and the bias-shifted AP data.

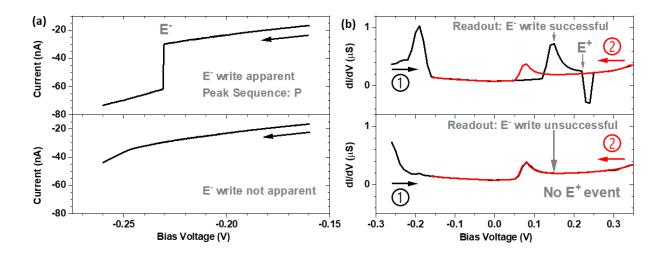
In the main text, we present evidence at V>0 of a shift to higher bias values of the Coulomb blockade peaks when the MTJ's magnetic state is switched from P to AP. We now consider the case of V<0, and focus on the Coulomb blockade peak shown in Suppl. Fig. S3. Its presence can also be switched on/off thanks to writing events E+ and E-, leading to different values of TMR at that bias position (see Fig. 2 of the main text). The data of Suppl. Fig. S3 is acquired within -100 < V (mV) < 0, i.e. below the writing events E- and E+ (see inset). An excellent overlap between the P and AP data is seen for bias value below the peak. However, as the peak onset is reached, a bias shift is clearly seen. The very close agreement in the data for the forward and reverse scans underscores that the shift is not the result of trivial charging/heating effects. To qualitatively estimate the small bias shift between the P and AP data, we manually shift the AP data. A reasonable fit is found for a bias shift of 0.35mV.

Note 3: Statistics on the memristive effect



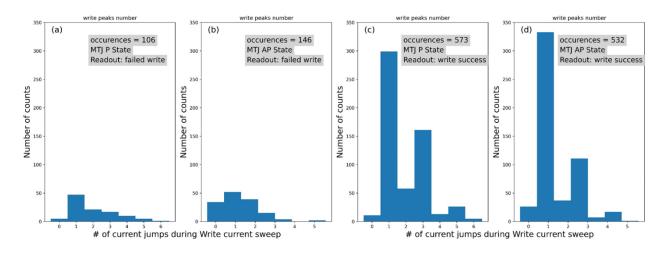
Suppl. Fig. S4: **Overview of the memristive Coulomb diamond shift.** (left) Differential conductance dI/dV vs. bias voltage on junction G10 at 10K. Successive data branches are shifted by 2μ S. The E+ and E-writing events cause a shift Δ_W =73mV in the constant Coulomb gap Δ_{CG} =310mV. (Right) Proposed energy diagram of the readout QD in the two E- and E+ states. The justification is provided in the discussion to Suppl. Fig. S8.

In the main text, we discuss how current jumps can displace the bias position of pairs of peaks associated with the Coulomb blockade diamond. In this note, we consider the statistics of this electric field-induced shift in the Coulomb diamond. To do so, we first plot an overview of the memristive Coulomb blockade effect in Suppl. Fig. S4. We observe that successive forward and reverse branches reveal a set of two conductance peaks separated by the same $\Delta_{CG} = 310$ mV. The E+ and E- writing events cause a shift $\Delta_W = 73$ mV in this pair of conductance peaks.



Suppl. Fig. S5: **Protocol to test junction state writing.** (a) Examples of IV traces showing E- write events that are (top) apparent, with 1 write peak observed, and (bottom) not apparent, i.e. with no write peak observed. (b) Corresponding readouts, with (top) confirmation and (bottom) information that the E-event-driven junction state was written.

To obtain statistical data on the ability to write a junction state, we undertook 1357 measurements on junction C5 at 10K. Examples of the write and read protocols are show in Fig. S.5. In general, attempting to activate the E- write event at negative bias generates a 81% success rate in the readout at positive bias. As we explain later, this success rate would likely increase if the maximum voltage of the writing IV protocol had been increased.



Suppl. Fig. S6: Statistics on the success and failure to write the junction state. The repeated protocol shown in SI Fig. S5 was used. The statistics are shown as a function of the number of current jumps during the Write current sweep.

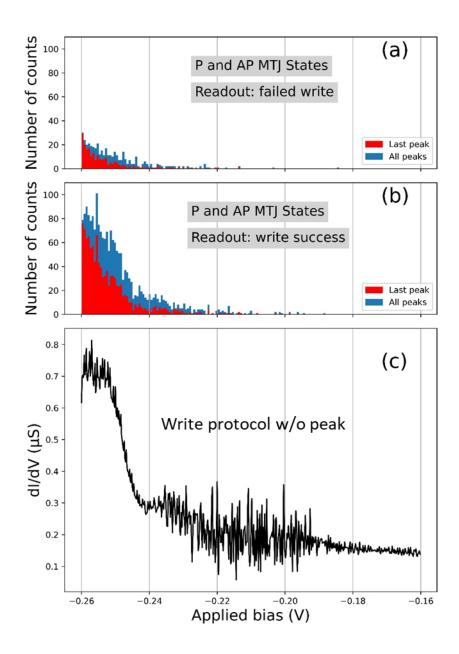
Referring to Suppl. Fig. S6, we note that the failure to write event E- in the MTJ's P state occurs mostly for one current jump, whereas it is spread over 0-2 jumps for the AP state. There are many AP write attempts without a current jump. Furthermore, for both P and AP MTJ states, cases with an odd number of current jumps dominate even cases.

Current Jump sequence (1 st Last)	Write Failed: # events	Write OK: # events	Write Success (%)
PN	57	93	62
PNPN	14	20	59
PNPNPN	2	2	50
P	88	548	86
PNP	32	271	89
PNPNP	5	43	90
PNPNPNP	1	4	80
No jump	39	37	49

Suppl. Table S1: Statistics of write success/failure according to the sequence of absolute current increase (P) and decrease (N).

To obtain more insight, we examine the sign of current change and current peak sequences in the entire dataset. We observe that:

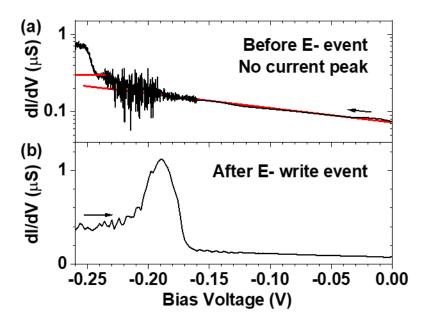
- if there is a peak, the first peak is always P. This means that the first current jump is always to more negative current values.
- the sign of succeeding current peaks is always opposite, i.e. there isn't a single PP or NN sequence or subsequence in our entire dataset.
- an odd number of current jumps (i.e. ending in P) has an overall success rate of 87%. This decreases to 61% for an even number of jumps (i.e. ending in N).



Suppl. Fig. S7: **Spectroscopy of current jumps.** Bias dependence of the frequency of a current jump when the writing event (a) fails and (b) succeeds. (c) Bias dependence of junction conductance when no current jump was observed. The average of 60 AP datasets is shown.

We compare in Suppl. Fig. S7 the bias dependencies of the baseline dI/dV for the junction's E+ state (i.e. without a current jump / conductance peak), and of the current jump event frequency. We observe that

almost all current jump events occur within the bias range at which a clear conductance increase is observed. We note that the successful write events mimick most closely this dependence/amplitude, while the failed current increase events occur mainly near the peak height. Conversely, very few current jumps, whether successful or not in promoting the E- writing event, are found within the -0.242 < Bias (V) < -0.188 range that exhibits transport noise. We conclude that, for this junction state, the E- writing event begins with the charging of the transport quantum dot, and not with a charging of the environmental quantum dot.



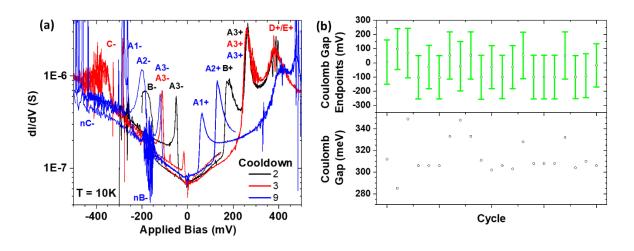
Suppl. Fig. S8: **Origin of transport noise prior to E- event.** (a) dI/dV traces in E+ state prior to E- event. Data with no current peak was chosen. The use of the log scale removes negative jumps. The average of 60 scans in the AP MTJ state were used. (b) dI/dV in E- state. Arrows indicate the direction of data acquisition.

We plot in Suppl. Fig. S8(a) dI/dV traces before the E- event, for which no current peak occurs. We observe an exponential increase in junction conductance starting from V=0, up to the onset of the very noisy - 0.242 < Bias (V) < -0.188 range (red line). Assuming that the conductance exponential increase were to remain the same across this noise range, we see that the conductance at V = 0.242 V would be half that measured (straight red line). We conclude that, in this particular junction state, the quantum interference transport between the readout quantum dot and the environmental quantum dot generates a net increase in current, i.e. that the environmental QD participates in transport through higher-order processes.

To verify that readout and environmental QDs with a fortuitously same Coulomb gap (see Suppl. Fig. S4(a)) are not simply trading roles in the E- and E+ events, we plot in panel (b) the dI/dV trace after a successful E- write event. We see that this trace's conductance peak does not have a bias range that matches that for the noise seen in panel (a). Furthermore, the two spectral features do not have the

same bias extent. This suggests that the E- and E+ events do not promote different readout QDs, but that the same QD remains as readout, but with an energy landscape that is shifted by the charging of the environmental QD (see Suppl. Fig. S4(b)). The bias extent and noise envelope of this environmental QD resembles the conductance peak of QD B, but with a +35meV energy shift.

Note 4: Overview of the several Coulomb gaps with evolving junction state and argumentation for single-atom 'transport' and 'environmental' quantum dots



Suppl. Fig. S9: **Overview of Coulomb gap energies with evolving junction state.** (a) Select dI/dV traces for three cooldowns. (b) (top) Endpoints of the Coulomb gap for select datasets deduced from the bias spacing of pairs of conductance peaks. (bottom) The resulting Coulomb energy gap of the transport atom. Junction G10 was used. The data from four cooldowns was used.

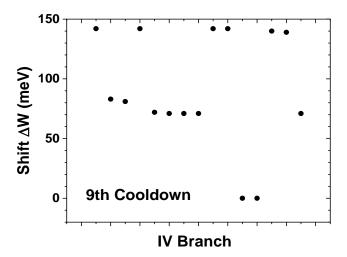
In our datasets, we observe that heating/cooling our FeCoB/MgO/C/MgO/FeCoB junctions, and bias cycling, can alter the effective potential landscape inferred at T=10K from the current derivative. To illustrate these effects, we focus on junction G10. We plot in Suppl. Fig. S9(a) select dl/dV traces obtained after three cooldowns. We have looked for a pattern of pairs of peaks with the same energy spacing as thermal and electrical cycling were conducted. This led us to label pairs of peaks and ascribe them to the charging of a given C atom. In total we identify at least 3, and as many as 5, atoms involved in the device's electrical response. As described in the main text, these atoms can be in the main transport path. In that case, charging the atom generates a conduction peak. Alternately, the atom in question can be tunnel coupled to a C atom that is in the transport path, and thus constitutes an 'environmental' atom. Following the deductions of Suppl. Fig. S9 and accompanying text, we assumed that energy motion of a pair of peaks was due to changes in the environmental charge felt by the transport atom, rather than the reattribution of 'transport' and 'environmental' roles. This logic is supported by the fairly stable energy gap between the paired peaks (see Suppl. Fig. S9(b)).

Using this labelling logic, we find for example, for cooldown #9, that pairs of conductance peaks can be attributed to the same carbon atom A, and that, in the course of IV cycling, three absolute energy positions of its Coulomb gap (see labels A1-, A2-, A3- and A1+, A2+ and A3+ in Suppl. Fig. S9(a)) relative to the MTJ electrodes' Fermi level can be tracked as the environmental charge is varied through write events E+ and E- (see main Text). Note how after an E+ writing event the pair of peaks shifts to lower absolute bias. The reverse occurs for an E- writing event. This trend in the bias shift was systematically observed, when a shift indeed occurred (see SI Note 2).

We observe additional conductance peaks at higher absolute bias voltage. In the absence of a clear trend suggesting additional charging of atom A, we surmise that these peaks correspond to additional atoms (C, D...) directly in the transport path.

Comparing these cooldowns, we observe that the peak of a dl/dV in one cooldown can spectrally correspond to noise for another cooldown. The best example is, at V^{-190} mV, that of peak B- in cooldown 2 (black), and of the corresponding noise nB- in cooldown 9 (blue). We infer that atom B is present in the transport path in cooldown 2, but becomes an environmental atom in cooldown 9. This also explains the absence of peaks B- and B+ in cooldowns 3 and 9.

We also observe that, in the junction state defined by cooldowns 3 and 9, the writing event E+ occurs just as the spectral window B+ corresponding to environmental atom B is reached with increasing positive bias around +150 mV. This illustrates the role that the charge state of environmental atom has in the junction write process (see main text).



Suppl. Fig. S10: **Quantization of the energy shift of the transport atom's Coulomb gap.** Absolute values are shown.

Within the junction state defined by a cooldown, writing events E- and E+ generate an effective bias shift that can be quantized. A ~75meV shift was observed on transport atom A during the 1357 tests of the E- and E+ event after cooldown 10 (see SI Note 2). A shift of 111meV was observed on atom B in a

transport role, However, those junction states promoted only two pairs of peaks. We present in Suppl. Fig. S10 the energy shift ΔW data in junction cooldown 9 arising from the presence of 3 pairs of peaks due to transport atom A. Aside from the trivial ΔW =0 points due to write failure (see SI Note 2), DW takes on multiple values of 70-80meV. Here, we make the reasonable assumption that the charge of an environmental atom can only change by 1 electron, which implies that several environmental atoms can be charged during a write event.

Note 5: Estimation of the impurities sizes and distances

Let us approximate the impurity involved in transport as a sphere of radius r, located at a distance d from the lower electrode, with interelectrode spacing l. In the far-field limit, the capacitance C is given in Ref. 1 and reads:

$$C = \frac{4\pi\epsilon\epsilon_0 r}{1 + (\psi^{(0)}(\frac{d}{l}) + \psi^{(0)}(1 - \frac{d}{l}) + 2\gamma)\frac{r}{2l}},$$

where $\,\psi^{(0)}$ is the polygamma function. Using the relation between the capacitance and the charging energy $E_C=e^2/2C=e\Delta_{CG}$, we obtain the radius of the impurity

$$r = \frac{l}{8\pi\epsilon\epsilon_0 \Delta_{CG}/e + 5/3}$$

where $\frac{1}{2}(\psi^{(0)}(d/l)+\psi^{(0)}(1-d/l)+2\gamma)\approx -5/3$ with d=1 nm and l=3 nm as approximated from the experimental design of the stack. Taking $\epsilon=9$ for the relative permittivity of MgO according to Ref. 2, we obtain r=0.2 nm. This shows that the impurities involved in the transport are of atomic sizes and should indeed correspond to single carbon atoms or dimers trapped inside the MgO lattice.

Let us now approximate both the transport and environmental quantum dots as two spheres of radius *r*, separated by a distance *d*. The capacitance *C* of the system is approximately given by:

$$C = \frac{2\pi\epsilon_0\epsilon r}{1 - \frac{r}{d-r}}$$

According to the observed shift $\Delta_W = 70$ mV which shall be due to the change of charge of one environmental quantum dot by a quantum of elementary charge, we should then write:

$$e = C\Delta_W$$

which leads to the distance between the dots:

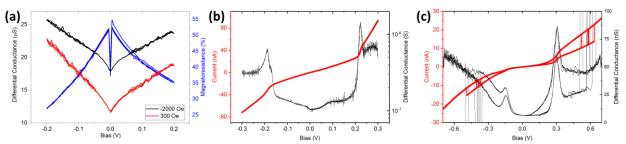
$$d = r \left(1 + \frac{1}{1 - \frac{2\pi\epsilon\epsilon_0 r \Delta_W}{e}} \right).$$

With r = 0.2 nm as estimated above; we obtain the following approximation:

$$d \approx 2r$$
 ,

such as d = 0.4 nm. We thus find that the distance between the transport quantum dots and the environmental charging species is of the order of the diameter of the dots, so the control dot should be a second, third or forth neighboring site of the transport dot in the MgO lattice. This estimation confirms that we are indeed observing the interaction of a reduced number of atomic formations closely packed inside the MgO barrier which are producing single-electron effects.

Note 6: Other junctions

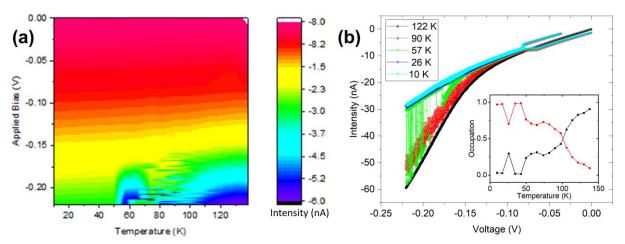


Suppl. Fig. S11: Magnetotransport experiments on other junctions. (a) Differential Conductance for the P (black) and AP (red) states and TMR (blue) plots at 10 K for junction F10. (b) and (c) Intensity-potential (black) and differential conductance (red) plots at 10 K and -2000 Oe for junctions B11 and B5 respectively.

Magnetoresistive properties have also been measured on several of these junctions, of the same kind as G10 and C5 presented in the main text. SI Fig.S11(a) shows that the electrical intensity of the junction F10 differs between the P and the AP configurations of the electrodes. This results in an apparent magnetoresistance of up to 60% that is maximal around 0. The conductance plot features two singular characteristics. First, the V-shaped spike around 0 mV, referred as the Zero-Bias anomaly (ZBA) [3-5], may indicate that an impurity state close to the Fermi level is located inside the MgO barrier [6]. This ZBA seems more pronounced in the P state than in the AP state as the deviation from linearity is more present at -2000 Oe in SI Fig.S11(a). Then, the noise visible in the linear part of the conductance, above 50 mV and below 50 mV should indicate the presence of two or more states close in energy which would result in several interfering nanotransport paths. An asymmetry is also observed in this figure: at negative bias the conductance is higher than at positive bias, in particular in the AP state which suggests that a structural asymmetry renders the electrodes nonequivalent. The drop in the junction resistance with increasing bias voltage is greater for antiparallel alignment of the magnetic electrodes than for parallel alignment which has been accounted for by spin excitations localized at the interfaces between the electrodes and the tunnel barrier [3].

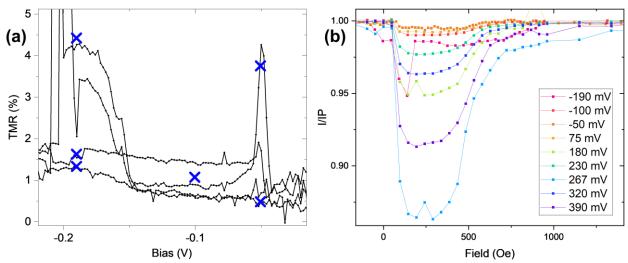
Of the 58 devices which have been tested, four other junctions displayed memristive behaviors, similar to G10 and C5, containing branch jumps and conductance peaks (see Figure SI Fig.S11(c)) which suggests the potential reproducibility of this phenomenon. Five other junctions also presented non-linear intensity-potential characteristics (see SI Fig.S11(b)) translating into sharp conductance peaks, but without branch jumps, looking more like standard MgO junctions without Carbon inside, but with a lower magnetoresistance.

Note 7: Memristance and temperature dependance



Suppl. Fig. S12: **Temperature dependance of the memristive behavior.** (a) Color plot of the current as a function of the temperature and applied bias for junction G10. (b) Intensity-Voltage characteristic of junction G10 recorded at five different temperatures. Inset: occupation probability of the low (in red) and high (in black) absolute intensity branches as a function of temperature.

Note 8: Magnetoresistance



Suppl. Fig. S13: **Magnetoresistance.** (a) Plot of the tunnel magnetoresistance as a function of the bias calculated from the intensity-voltage characteristic in the P and AP states of junction G10. The blue crosses represent points that have been confirmed by I(H) experiments. The TMR enhancement due to the different memristive Coulomb blockade peaks can be observed. (b) Relative intensity compared to the P state as a function of the external field for different applied bias obtained from junction G10.

[1] A. M. Drews, M. Kowalik, and K. J. M. Bishop, "Charge and force on a conductive sphere between two parallel electrodes: A Stokesian dynamics approach," *Journal of Applied Physics* 116, 074903 (2014).
[2] D. R. Lide, G. Baysinger, S. Chemistry, L. I. Berger, R. N. Goldberg, and H. V. Kehiaian, "CRC Handbook of Chemistry and Physics".

[3] S. Zhang, P. M. Levy, A. C. Marley, and S. S. P. Parkin, "Quenching of Magnetoresistance by Hot Electrons in Magnetic Tunnel Junctions," *Physical Review Letters* 79, 3744–3747 (1997).

[4] A. F. G. Wyatt, "Anomalous Densities of States in Normal Tantalum and Niobium," *Physical Review Letters* 13, 401–404 (1964).

[5] J. A. Appelbaum and L. Y. L. Shen, "Zero-Bias-Conductance Peak Anomaly of Ta- I -Al Tunnel Junctions at 0.3 K and 90 kG," *Physical Review B* 5, 544–553 (1972).

[6] G.-X. Miao, M. Münzenberg, and J. S. Moodera, "Tunneling path toward spintronics," *Reports on Progress in Physics* 74, 036501 (2011).

[7] https://lmfit.github.io/lmfit-py/